Geochemical Perspectives Letters

Iron(III) reducing bacteria immobilise antimonite by respiring elemental sulfur

L. Ye[1], C. Jing[1,2*]

OPEN ACCESS

https://doi.org/10.7185/geochemlet.2215

Abstract

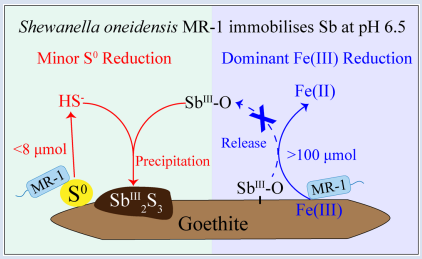

Iron(III) reducing bacteria (IRB) are best known and most influential drivers for mobilising metal(loid)s *via* reductive dissolution of iron(III)-containing minerals. Our study challenges this preconception and found that IRB immobilise metal(loid)s by respiring elemental sulfur (S^0) even when Fe(III) reduction is prevailing under mildly acidic conditions. Antimony (Sb), a toxic contaminant, was chosen as an example of metal(loid)s. Antimonite-adsorbed goethite was incubated with *Shewanella oneidensis* MR-1, a widely distributed IRB, in the presence of S^0 at pH 6.5. The results show that although the extent of Fe(III) reduction (>100 µmol) was over ten times greater than that of S^0 reduction (<8 µmol), it was S^0 reduction that immobilised Sb through Sb_2S_3 precipitation. Further, the thermodynamic calculation suggests that such great impacts of marginal S^0 reduction can be extended to other metal(loid)s *via* the formation of soluble thio-species or sulfide precipitates. This study redefines the role of IRB in the environmental fate of metal(loid)s, highlighting the strong impacts from the marginal S^0 reduction over the central Fe(III) reduction.

Received 23 December 2021 | Accepted 3 March 2022 | Published 5 May 2022

Introduction

Iron oxides are natural scavengers for toxic metal(loid)s and iron reducing bacteria (IRB) mobilise these metal(loid)s by facilitating the reductive dissolution of iron oxides (Kappler *et al.*, 2021). For example, elevated arsenic (As) (Kontny *et al.*, 2021), antimony (Sb) (Hockmann *et al.*, 2014), mercury (Hg) (Wang *et al.*, 2021) and cadmium (Cd) (Zhou *et al.*, 2020) in waters usually associate with increasing Fe(II) concentrations in the presence of IRB. In fact, many IRB, such as *Shewanella* and *Geobacter* spp., have an underappreciated ability: elemental sulfur (S^0) respiration (Flynn *et al.*, 2014). Accordingly, the biogenic sulfide (HS^-) may either immobilise metal(loid)s *via* sulfide precipitates or mobilise them by forming soluble thio-species (Planer-Friedrich *et al.*, 2020; Ye *et al.*, 2020; Helz, 2021). Previous studies suggested that S^0 is widely distributed in sediments and waters, and its concentration can be as high as 60 mM as summarised in Table S-1. S^0 usually co-exists with Fe(III) oxides in the environment where FeS oxidation occurs (Burton *et al.*, 2009) or where microbial sulfate reduction occurs in the presence of Fe(III) oxides (Burton *et al.*, 2011). Thus, rather than Fe(III) reduction alone, IRB influence the mobility of metal(loid)s *via* coupled Fe(III) and S^0 reduction.

The extents of Fe(III) and S^0 reduction reveal their contribution in regulating the fate of metal(loid)s. Our recent work found that IRB prefer to reduce S^0 under mildly alkaline conditions, and the biogenic sulfide greatly enhanced Sb release by the formation of thioantimonates (Ye *et al.*, 2022). In contrast, in the acidic environments, IRB prefer to respire Fe(III) rather than S^0 to conserve more energy (Flynn *et al.*, 2014). The effect of S^0 respiration by IRB is previously neglected and probably masked by appreciable Fe(III) reduction on the fate of metal(loid)s. Thus, prevailing Fe(III) reduction (Cummings *et al.*, 2000) is commonly considered to drive the mobility of metal(loid)s in mildly acidic sediments (Hockmann *et al.*, 2015), such as mining areas and acidic wetlands (Karimian *et al.*, 2018).

Contrary to the previous preconception, our study revealed that S^0 respiration by IRB even to a marginal extent can greatly shape the fate of metal(loid)s under mildly acidic conditions. In detail, antimony (Sb), an emerging contaminant, is chosen as an example of metal(loid)s. Antimonite-adsorbed goethite was incubated with *Shewanella oneidensis* MR-1, a typical Fe(III) reducing bacterium, in the presence of S^0 at pH 6.5. Our incubation and characterisation results suggest that although Fe(III) was the dominant electron acceptor and Fe(III) reduction was over ten times greater than S^0 reduction, Sb release was mainly inhibited by biogenic sulfide through the formation of Sb_2S_3 precipitates. The thermodynamic calculation further indicates that the strong effect of marginal S^0 reduction can be extended from Sb to other metal(loid)s. This study breaks the stereotype that IRB influence the mobility of metal(loid)s *via* Fe(III) reduction alone, and highlights the importance of S^0 respiration.

Materials and Methods

The experiments were performed at pH 6.5 in the dark, and the experimental setup and analytical techniques were similar to our previous study (Ye *et al.*, 2022). Dissolved Fe(II), sulfide,

1. Shandong Key Laboratory of Environmental Processes and Health, School of Environmental Science and Engineering, Shandong University, Qingdao 266237, China
2. State Key Laboratory of Environmental Chemistry and Ecotoxicology, Research Center for Eco-Environmental Sciences, Chinese Academy of Sciences, Beijing 100085, China
* Corresponding author (email: cyjing@rcees.ac.cn)

antimonite, antimonate and thioantimonates were analysed periodically during the incubation. To extend the effect of marginal S^0 reduction from Sb to other metal(loid)s, reaction path models were established to calculate the species of Sb, arsenic (As), tungsten (W), molybdenum (Mo), mercury (Hg), lead (Pb), zinc (Zn), cadmium (Cd) and copper (Cu) as a function of pH and the activity of sulfide in the presence of goethite. More details of the methods are shown in the Supplementary Information (SI).

Results and Discussion

Prevalent Fe(III) reduction versus minor S^0 reduction. During the incubation with *Shewanella oneidensis* MR-1 at pH 6.5 (Fig. S-2), the electron donor was formate and the electron acceptor was either goethite or S^0. To determine the dominant electron acceptor in our experiments, dissolved Fe(II) and sulfide (HS^-) were measured (Fig. 1) and the electrons accepted by goethite or S^0 were calculated (Table S-2). In the abiotic control without MR-1 (Goe-Sb^{III}+S^0), Fe(II) and sulfide were not detected (Fig. 1). In the presence of MR-1 (MR-1+Goe-Sb^{III}+S^0), dissolved Fe(II) concentrations reached up to 527 ± 27 μM whereas sulfide was below 3 μM during the 192 hr incubation (Fig. 1a). Such a low sulfide concentration (<3 μM) would have a negligible effect on goethite reduction (Poulton *et al.*, 2004). At the end of incubation, 2.7 ± 0.5 μmol/g Fe(II) were adsorbed on solids and 26.6 ± 3.4 μmol/g sulfide were precipitated (Table S-2). Overall, goethite accepted 106.1 ± 5.3 μmol electrons from MR-1 while S^0 accepted 14.4 ± 1.6 μmol. The order of magnitude difference in electrons suggested that goethite was the dominant electron acceptor at pH 6.5.

Consistent with the prevailing Fe(III) reduction, the thermodynamic calculations show that the free energy gain (ΔG_r) with goethite as the electron acceptor is higher than that with S^0 (Fig. S-3), as detailed in SI. Previous studies also suggested that microbial Fe(III) reduction is the central pathway in acidic environments under anoxic conditions, and IRB are the dominant bacteria therein (Sun *et al.*, 2015). Inconsistent with the redox ladder concept (Peiffer *et al.*, 2021), minor S^0 reduction still occurred although in a lower ΔG_r than goethite. However, no research has paid attention to the marginal S^0 reduction by IRB in acidic environments.

Minor S^0 reduction immobilises Sb. As a primary pathway, Fe(III) reduction has been reported to enhance Sb release due to a depletion of sorption sites (Hockmann *et al.*, 2014); however, the concentration of total dissolved Sb decreased from 9.07 ± 0.48 μM to 0.19 ± 0.07 μM in MR-1+Goe-Sb^{III}+S^0 (Fig. 1b). In the abiotic control (Goe-Sb^{III}+S^0; Fig. 1c), the Sb concentration slightly increased from 7.33 ± 0.27 μM to 8.95 ± 0.57 μM during the incubation. The dissolved Sb was mainly Sb^{III}-O, and no thiolated Sb species was detected by IC-ICP-MS (Fig. 1b-c). The decrease in dissolved Sb in MR-1+Goe-Sb^{III}+S^0 was consistent with the loss of Sb^{III}-O (Fig. 1b).

The loss of dissolved Sb^{III}-O in MR-1+Goe-Sb^{III}+S^0 was due to the formation of Sb_2S_3 as evidenced by Sb L_I-edge XANES analysis (Figs. 2a, S-4 and Table S-4). In detail, the first derivative peak at 4703 eV in Goe-Sb^{III}+S^0 was attributed to Sb^{III}-O, in accordance with the initial Sb^{III}-O adsorbed on goethite (Fig. 2a). In the presence of MR-1, Sb^{III}-O was transformed to Sb_2S_3 at 4702 eV (Fig. 2a). Linear combination fitting (LCF) of XANES spectra further confirmed that 36 ± 4 % Sb_2S_3 were formed in MR-1+Goe-Sb^{III}+S^0, whereas the proportion of Sb_2S_3 in Goe-Sb^{III}+S^0 (5 ± 2 %) was negligible (Table S-4). In addition, approximately 51 ± 1 % and 39 ± 2 % Sb^{III}-O were oxidised to antimonate (Sb^V-O) in Goe-Sb^{III}+S^0 and MR-1+Goe-Sb^{III}+S^0, respectively (Fig. 2a and Table S-4). The abiotic oxidation was ascribed to the electron transfer between Sb^{III}-O and goethite (Yin *et al.*, 2021), as detailed in SI.

The mass balance calculations show that 1.52 ± 0.62 μmol Sb^{III}-O were precipitated in the presence of MR-1 at the end of incubation, but 4.30 ± 0.48 μmol Sb as Sb_2S_3 were detected by XANES analysis. The much higher amount of Sb as Sb_2S_3 than the loss of dissolved Sb^{III}-O suggests that not only dissolved, but also adsorbed Sb^{III}-O, reacted with biogenic sulfide to form Sb_2S_3 precipitates. Consistent with this observation, the precipitation of Sb_2S_3 may readily occur in mildly acidic environments, such as paddy soils, wetland, groundwater and lake/river systems where sulfide was commonly less than 10 μM (Figs. 3a, S-6a). Actually, if sulfide or pH slightly increased, instead of Sb_2S_3, soluble thioantimony (Sb-S) would be prevalent (Figs. 3a, S-6a), resulting in enhanced Sb release (Ye *et al.*, 2022).

Unlike our results, a previous study ascribed the immobilisation of Sb to incorporation of Sb^V-O into the newly formed secondary iron phases (*i.e.* feroxyhyte and goethite) (Burton *et al.*, 2019). However, that pathway is not suitable in our system because the phase transformation of goethite was not significant. In detail, Fe XANES LCF analysis suggest that 99 ± 0 % of Fe phases remained as goethite and negligible iron sulfides (1 ± 1 % of total Fe) were formed at the end of incubation (Fig. S-5 and Table S-5). S K-edge XANES also confirmed the negligible formation of iron sulfides (4 ± 1 % of total S; Fig. S-5 and Table S-6). The newly formed iron sulfide may co-precipitate with or re-adsorb Sb, but its low content (1 ± 1 % of total Fe) limited its contribution to Sb mobility (detailed in SI).

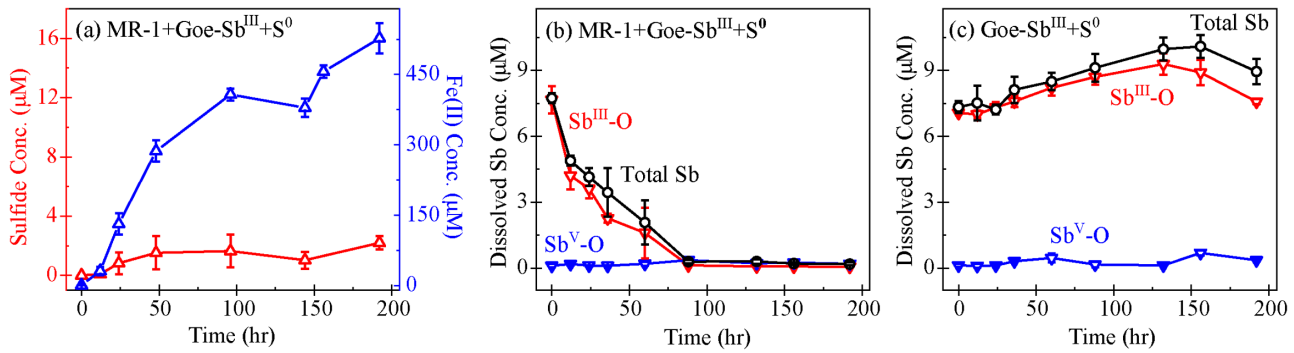

Figure 1 **(a)** Changes in dissolved sulfide (red) and Fe(II) (blue). **(b)** Total dissolved Sb (black), Sb^{III}-O (red), and Sb^V-O (blue) during incubation in MR-1+Goe-Sb^{III}+S^0 at pH 6.5. **(c)** Changes in dissolved Sb species in abiotic control Goe-Sb^{III}+S^0. Fe(II) and sulfide were not detected in Goe-Sb^{III}+S^0.

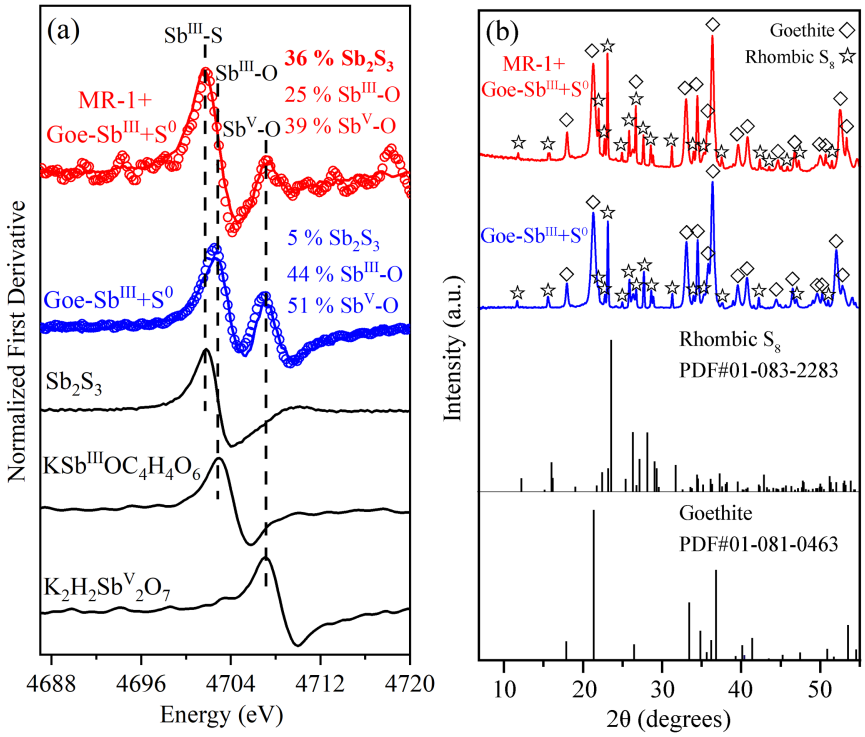

Figure 2 **(a)** Observed (circles) and linear combination fitting (lines) for the first derivative of normalised Sb L_I-edge XANES for samples at the end of incubation. Spectra for standard references are also shown for comparison. The results of linear combination fitting analysis are shown in Table S-4. **(b)** Synchrotron X-ray powder diffraction pattern recorded from the solid in MR-1+Goe-Sb^{III}+S^0 and Goe-Sb^{III}+S^0 at the end of incubation.

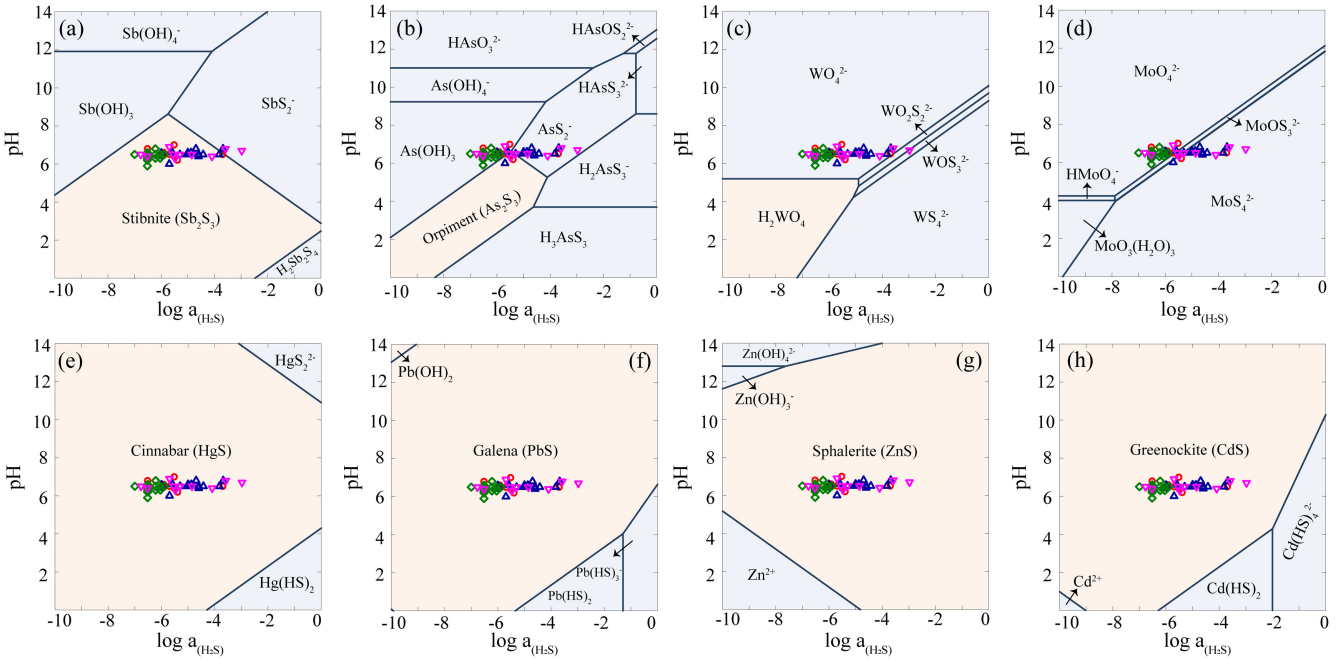

Figure 3 Species of **(a)** Sb, **(b)** As, **(c)** W, **(d)** Mo, **(e)** Hg, **(f)** Pb, **(g)** Zn and **(h)** Cd in the reaction with different log activity (H_2S) and pH values in the presence of goethite at 25 °C. The activities of these metal(loid)s were set as 10 μM. The red, blue, green and magenta symbols represent the sulfide concentrations in mildly acidic paddy, wetland, groundwater and lake/river systems, respectively. The data are from references in Table S-7.

In addition, synchrotron X-ray diffraction (SXRD) did not resolve new Fe minerals other than goethite and rhombic S_8 in both Goe-Sb^{III}+S^0 and MR-1+Goe-Sb^{III}+S^0 samples at the end of incubation (Fig. 2b).

A recent study demonstrated that Sb^V-O can readily incorporate into the goethite structure during Fe(II) catalysed recrystallisation without phase transformation (Burton *et al.*, 2020). This phenomenon, which involves relatively rapid

interactions between goethite and Fe(II), may have contributed to the immobilisation of Sb under our experimental conditions. However, an assessment of the quantitative contribution of Fe(II)-induced goethite recrystallisation to Sb immobilisation in our experiment is beyond the scope of the present study. Despite this possible uncertainty, it is clear from our results that a substantial amount of Sb was certainly immobilised *via* Sb_2S_3 precipitation due to the IRB-driven S^0 reduction.

Strong impacts from weak S^0 reduction on metal(loid)s mobility. Since environmental acidification is inevitable with increasing CO_2 emission (Terhaar *et al.*, 2020), the effect of marginal S^0 reduction under mildly acidic conditions should be paid more attention. This effect can be extended to other metal(loid)s including arsenic, tungsten, molybdenum, mercury, lead, zinc and cadmium. To justify the proposition, reaction path modelling was performed to predict the speciation change of these metal(loid)s at 10 μM (Fig. 3) and 1 μM (Fig. S-6) as a function of pH and the activity of sulfide. As shown in our thermodynamic calculations (Figs. 3b-d, S-6b-d), soluble thiolated species such as thioarsenic (As-S), thiotungsten (W-S), and thiomolybdenum (Mo-S) would occur in multiple low sulfide (<0.1 mM) environments. Consistent with our results, As-S has been detected in paddy soil porewaters when sulfide <10 μM at pH 6.5, and the As-S formation was promoted by S^0 (Wang *et al.*, 2020). In general, the formation of As-S and W-S may enhance their mobility (Mohajerin *et al.*, 2014; Ye *et al.*, 2020), whereas Mo-S is less mobile than Mo-O due to its higher affinity for sulfide minerals and natural organic matter (Smedley and Kinniburgh, 2017).

On the other hand, S^0 reduction leads to precipitation of sulfide minerals, such as cinnabar (HgS), galena (PbS), sphalerite (ZnS), and greenockite (CdS) (Figs. 3e-h, S-6e-h). These minerals immobilise metal(loid)s due to minor S^0 reduction (~10 μM), resulting in decoupling of Fe(II) and metal(loid)s release to the aqueous phase during the microbial Fe(III) reduction. However, most previous studies attributed the decoupling of Fe(II) and metal(loid)s release to re-adsorption on, or incorporation into, the newly formed iron minerals (Hockmann *et al.*, 2020). This study provides a new perspective that IRB shape the mobility and transformation of metal(loid)s *via* S^0 respiration. Even under mildly acidic conditions where Fe(III) reduction is prevailing, the underappreciated and marginal S^0 reduction plays a vital role in the mobility of metal(loid)s.

Author Contributions

LY conceived the study, performed the experiments, interpreted the data and wrote the first draft; CJ contributed to the work design, data interpretation and manuscript revision.

Competing interests:

The authors declare no competing financial interest.

Acknowledgements

We acknowledge the financial support of the National Natural Science Foundation of China (41877378 and 41425016), the China Postdoctoral Science Foundation (2021M691924), and the Natural Science Foundation of Shandong Province, China (ZR2020ZD34, ZR2021QD054).

Editor: Andreas Kappler

Additional Information

Supplementary Information accompanies this letter at https://www.geochemicalperspectivesletters.org/article2215.

Cite this letter as: Ye, L., Jing, C. (2022) Iron(III) reducing bacteria immobilise antimonite by respiring elemental sulfur. *Geochem. Persp. Let.* 21, 37–41. https://doi.org/10.7185/geochemlet.2215

References

Burton, E.D., Bush, R.T., Sullivan, L.A., Hocking, R.K., Mitchell, D.R.G., Johnston, S.G., Fitzpatrick, R.W., Raven, M., McClure, S., Jang, L.Y. (2009) Iron-monosulfide oxidation in natural sediments: Resolving microbially mediated S transformations using XANES, electron microscopy, and selective extractions. *Environmental Science & Technology* 43, 3128–3134. https://doi.org/10.1021/es8036548

Burton, E.D., Bush, R.T., Johnston, S.G., Sullivan, L.A., Keene, A.F. (2011) Sulfur biogeochemical cycling and novel Fe-S mineralization pathways in a tidally re-flooded wetland. *Geochimica et Cosmochimica Acta* 75, 3434–3451. https://doi.org/10.1016/j.gca.2011.03.020

Burton, E.D., Hockmann, K., Karimian, N., Johnston, S.G. (2019) Antimony mobility in reducing environments: The effect of microbial iron(III)-reduction and associated secondary mineralization. *Geochimica et Cosmochimica Acta* 245, 278–289. https://doi.org/10.1016/j.gca.2018.11.005

Burton, E.D., Hockmann, K., Karimian, N. (2020) Antimony sorption to goethite: Effects of Fe(II)-catalyzed recrystallization. *ACS Earth and Space Chemistry* 4, 476–487. https://doi.org/10.1021/acsearthspacechem.0c00013

Cummings, D.E., March, A.W., Bostick, B., Spring, S., Caccavo, F., Fendorf, S., Rosenzweig, R.F. (2000) Evidence for microbial Fe(III) reduction in anoxic, mining-impacted lake sediments (Lake Coeur d'Alene, Idaho). *Applied and Environmental Microbiology* 66, 154–162. https://doi.org/10.1128/AEM.66.1.154-162.2000

Flynn, T.M., O'Loughlin, E.J., Mishra, B., DiChristina, T.J., Kemner, K.M. (2014) Sulfur-mediated electron shuttling during bacterial iron reduction. *Science* 344, 1039–1042. https://doi.org/10.1126/science.1252066

Helz, G.R. (2021) Dissolved molybdenum asymptotes in sulfidic waters. *Geochemical Perspectives Letters* 19, 23–26. https://doi.org/10.7185/geochemlet.2129

Hockmann, K., Lenz, M., Tandy, S., Nachtegaal, M., Janousch, M., Schulin, R. (2014) Release of antimony from contaminated soil induced by redox changes. *Journal of Hazardous Materials* 275, 215–221. https://doi.org/10.1016/j.jhazmat.2014.04.065

Hockmann, K., Tandy, S., Lenz, M., Reiser, R., Conesa, H.M., Keller, M., Studer, B., Schulin, R. (2015) Antimony retention and release from drained and waterlogged shooting range soil under field conditions. *Chemosphere* 134, 536–543. https://doi.org/10.1016/j.chemosphere.2014.12.020

Hockmann, K., Planer-Friedrich, B., Johnston, S.G., Peiffer, S., Burton, E.D. (2020) Antimony mobility in sulfidic systems: Coupling with sulfide-induced iron oxide transformations. *Geochimica et Cosmochimica Acta* 282, 276–296. https://doi.org/10.1016/j.gca.2020.05.024

Kappler, A., Bryce, C., Mansor, M., Lueder, U., Byrne, J.M., Swanner, E.D. (2021) An evolving view on biogeochemical cycling of iron. *Nature Reviews Microbiology* 19, 2679–2698. https://doi.org/10.1038/s41579-020-00502-7

Karimian, N., Johnston, S.G., Burton, E.D. (2018) Iron and sulfur cycling in acid sulfate soil wetlands under dynamic redox conditions: A review. *Chemosphere* 197, 803–816. https://doi.org/10.1016/j.chemosphere.2018.01.096

Kontny, A., Schneider, M., Eiche, E., Stopelli, E., Glodowska, M., Rathi, B., Göttlicher, J., Byrne, J.M., Kappler, A., Berg, M., Thi, D.V., Trang, P.T. K., Viet, P.H., Neumann, T. (2021) Iron mineral transformations and their

impact on As (im)mobilization at redox interfaces in As-contaminated aquifers. *Geochimica et Cosmochimica Acta* 296, 189–209. https://doi.org/10.1016/j.gca.2020.12.029

Mohajerin, T.J., Helz, G.R., White, C.D., Johannesson, K.H. (2014) Tungsten speciation in sulfidic waters: Determination of thiotungstate formation constants and modeling their distribution in natural waters. *Geochimica et Cosmochimica Acta* 144, 157–172. https://doi.org/10.1016/j.gca.2014.08.037

Peiffer, S., Kappler, A., Haderlein, S.B., Schmidt, C., Byrne, J.M., Kleindienst, S., Vogt, C., Richnow, H.H., Obst, M., Angenent, L.T., Bryce, C., McCammon, C., Planer-Friedrich, B. (2021) A biogeochemical–hydrological framework for the role of redox-active compounds in aquatic systems. *Nature Geoscience* 14, 264–272. https://doi.org/10.1038/s41561-021-00742-z

Planer-Friedrich, B., Forberg, J., Lohmayer, R., Kerl, C.F., Boeing, F., Kaasalainen, H., Stefánsson, A. (2020) Relative abundance of thiolated species of As, Mo, W, and Sb in hot springs of Yellowstone National Park and Iceland. *Environmental Science & Technology* 54, 4295–4304. https://doi.org/10.1021/acs.est.0c00668

Poulton, S.W., Krom, M.D., Raiswell, R. (2004) A revised scheme for the reactivity of iron (oxyhydr)oxide minerals towards dissolved sulfide. *Geochimica et Cosmochimica Acta* 68, 3703–3715. https://doi.org/10.1016/j.gca.2004.03.012

Smedley, P.L., Kinniburgh, D.G. (2017) Molybdenum in natural waters: A review of occurrence, distributions and controls. *Applied Geochemistry* 84, 387–432. https://doi.org/10.1016/j.apgeochem.2017.05.008

Sun, W., Xiao, T., Sun, M., Dong, Y., Ning, Z., Xiao, E., Tang, S., Li, J. (2015) Diversity of the sediment microbial community in the Aha watershed (southwest China) in response to acid mine drainage pollution gradients. *Applied and Environmental Microbiology* 81, 4874–4884. https://doi.org/10.1128/AEM.00935-15

Terhaar, J., Kwiatkowski, L., Bopp, L. (2020) Emergent constraint on Arctic Ocean acidification in the twenty-first century. *Nature* 582, 379–383. https://doi.org/10.1038/s41586-020-2360-3

Wang, J., Shaheen, S.M., Jing, M., Anderson, C.W.N., Swertz, A.-C., Wang, S.-L., Feng, X., Rinklebe, J. (2021) Mobilization, methylation, and demethylation of mercury in a paddy soil under systematic redox changes. *Environmental Science & Technology* 55, 10133–10141. https://doi.org/10.1021/acs.est.0c07321

Wang, J.J., Kerl, C.F., Hu, P.J., Martin, M., Mu, T.T., Bruggenwirth, L., Wu, G.M., Said-Pullicino, D., Romani, M., Wu, L.H., Planer-Friedrich, B. (2020) Thiolated arsenic species observed in rice paddy pore waters. *Nature Geoscience* 13, 282–287. https://doi.org/10.1038/s41561-020-0533-1

Ye, L., Meng, X., Jing, C. (2020) Influence of sulfur on the mobility of arsenic and antimony during oxic-anoxic cycles: Differences and competition. *Geochimica et Cosmochimica Acta* 288, 51–67. https://doi.org/10.1016/j.gca.2020.08.007

Ye, L., Zhong, W., Zhang, M., Jing, C. (2022) New mobilization pathway of antimonite: thiolation and oxidation by dissimilatory metal-reducing bacteria via elemental sulfur respiration. *Environmental Science & Technology* 56, 652–659. https://doi.org/10.1021/acs.est.1c05206

Yin, X.L., Zhang, G.Q., Su, R., Zeng, X.F., Yan, Z.L., Zhang, D.N., Ma, X., Lei, L., Lin, J.R., Wang, S.F., Jia, Y.F. (2021) Oxidation and incorporation of adsorbed antimonite during iron(II)-catalyzed recrystallization of ferrihydrite. *Science of The Total Environment* 778, 146424. https://doi.org/10.1016/j.scitotenv.2021.146424

Zhou, Z., Muehe, E.M., Tomaszewski, E., Lezama Pacheco, J., Kappler, A., Byrne, J.M. (2020) Effect of natural organic matter on the fate of cadmium during microbial ferrihydrite reduction. *Environmental Science & Technology* 54, 9445–9453. https://doi.org/10.1021/acs.est.0c03062

Geochemical Perspectives Letters

Iron(III) reducing bacteria immobilise antimonite by respiring elemental sulfur

L. Ye, C. Jing

Supplementary Information

The Supplementary Information includes:

- Materials and Methods
- Results and Discussion
- Tables S-1 to S-7
- Figures S-1 to S-6
- Supplementary Information References

Materials and Methods

1. Adsorption Experiments:

The preparation of Goe-Sb^{III} is similar to our previous study (Ye *et al.*, 2019). Antimonite (potassium antimony tartrate) was loaded on goethite (α-FeOOH) at 60 mmol/kg to simulate Sb content and species in natural contaminated subsurface sediments, labelled as Goe-Sb^{III}. In detail, $KSb^{III}OC_4H_4O_6 \cdot {}^1/_2H_2O$ (Sinopharm Chemical Reagent Co., Ltd) was dissolved in deoxygenated deionized (DI) water to prepare 10 mM Sb^{III}-O stock solution. The stock solution was filtered through a 0.22 μm sterile membrane filter to prevent bacterial contamination in the glovebox (100 % N_2). Goethite was autoclaved at 0.1 MPa and 121 °C for 20 min. Filtered Sb^{III}-O stock solution (0.6 ml) was simultaneously mixed with 0.1 g sterile goethite and diluted with DI water to 45 ml. The samples were mixed on a rotator in dark for 12 h, and then the suspensions after adsorption were filtered through 0.22 μm membrane filters to detect total dissolved Sb. The dissolved Sb concentration after adsorption was 0.2 μM. Finally, the goethite+Sb^{III}-O mixture was centrifuged and the solid phase was rinsed three times with autoclaved deoxygenated DI water.

2. Incubation Experiments:

Shewanella oneidensis MR-1 was activated in Luria-Bertani (LB) medium at 30 °C on an orbital shaker (160 rpm) for 24 h under aerobic conditions. After activation, cells of MR-1 in 30 mL LB medium were harvested at 8000 g (6000 rpm, Eppendorf 5424, Hamburg, Germany) for 5 min and washed by fresh sterile BTPGW three times. The cells were then inoculated anaerobically into 200 mL sterile buffered artificial groundwater (BTPGW) medium containing 1 g/L Goe-Sb^{III} solid and 0.32 g/L sterile powdered rhombic S_8, labelled as MR-1+Goe-Sb^{III}+S^0. Goethite and powdered rhombic S_8 were validated by X-ray powder diffraction as shown in Figure S-1. Abiotic controls without MR-1 inoculation were also prepared following the same procedures as the MR-1+Goe-Sb^{III}+S^0, labelled as Goe-Sb^{III}+S^0. Each system was performed in triplicates.

3. BTP-buffered artificial groundwater (BTPGW):

The recipe for preparing BTPGW (1 L): 10 mM bis-tris propane (BTP), 4.21 mM $CaCl_2$, 0.28 mM KCl, 1.11 mM $MgCl_2 \cdot 6H_2O$, 0.01 mM KH_2PO_4, 0.10 mM NH_4Cl, 5.05 mM $NaHCO_3$, 1 mM HCOONa, 10 mL vitamin solution, 1 mL SL-10 trace elements solution. The sterilisation of all components was realised by filtration or autoclavation. The culture medium was equilibrated under an 100 % N_2 atm, and the pH was adjusted to 6.5 with HCl.

4. Dissolved Fe, S and Sb species analysis:

During the incubation, the homogenised suspensions (~2.0 ml) were sampled periodically and then filtered through 0.22 μm membrane filters for soluble Fe, S and Sb speciation analysis. Dissolved sulfide and Fe(II) concentrations were analysed with the methylene blue method and the colourimetric 1,10-phenanthroline method, respectively(Clesceri *et al*., 1998). To exclude the impact of the BTPGW medium on sulfide and Fe(II) detection, the calibration curves of sulfide and Fe(II) were established based on the standards in the BTPGW matrix. The sorbed Fe(II) was determined by digestion of the solids in 0.4 M HCl (Yin *et al*., 2021), and the sulfide in the solid was determined by digestion with 5 M HCl first, and then trapping with 0.05 M NaOH (Zerkle *et al*., 2010).

Total dissolved Sb concentrations were determined by inductively coupled plasma-mass spectrometry (ICP-MS, NexION350X, PerkinElmer). Anion-exchange chromatography ICP-MS (IC-ICP-MS) and high-performance liquid chromatography (HPLC) coupled with ICP-MS were used to quantify the concentrations of dissolved Sb speciation (Ye *et al*., 2020). In detail, dissolved Sb species were separated by a DX-1100 ion chromatograph (IC, Dionex, Sunnyvale, CA) with an AG16/ AS16 IonPac column before quantification with ICP-MS. The mobile phase was 70 mM KOH with a flow rate of 1.2 mL/min. Due to the lack of available standards, thioantimonate species were quantified based on the calibration curve of antimonate (Sb^V-O). Because the IC peaks of Sb^V-O and antimonite (Sb^{III}-O) were partially overlapped, high-performance liquid chromatography (HPLC) coupled with ICP-MS was used to quantify the concentration of Sb^V-O as follows: a Hamilton PRP-X100 anion exchange column was used to separate Sb^{III}-O and Sb^V-O, and the mobile phase was 10 mM EDTA and 1 mM potassium-hydrogen phthalate (KHP) with a flow rate of 1.0 mL/min.

5. XANES analysis:

At the end of the incubation, the solids were collected by centrifugation at 16,000*g* (Eppendorf 5424, Hamburg, Germany), then washed with autoclaved DI water three times, and finally freeze-dried for X-ray absorption near edge structure (XANES) spectroscopic analysis. Sb L_I-edge, S and Fe K-edge XANES analysis were used to explore the Sb, Fe and S speciation in the solid, respectively. The spectra were recorded in fluorescence mode with a Lytle detector at room temperature on beamline 16A at the National Synchrotron Radiation Research Centre (NSRRC). The Sb and S spectra were collected under He atmosphere, and Fe spectra were collected under N_2 atmosphere. The Sb spectra were obtained from −35 to +250 eV relative to the Sb L_I-edge (4698 eV) with a step size of 0.2 eV at the edge region. The Fe K-edge XANES spectra were collected from −70 to +300 eV relative to the Fe K-edge (7112 eV) with a step size of 0.25 eV at the edge region. The S spectra were obtained from −200 to +200 eV relative to the S K-edge (2472 eV) with a step size of 0.2 eV at the edge region. Standard reference chemicals as shown in Figure 2a and Figure S5-S6 were also measured. Normalisation of the XANES spectra was conducted using the software Athena as used in our previous studies (Ye *et al*., 2020). XANES spectra were analysed using linear combination fitting (LCF) with the Athena program.

6. SXRD Analysis:

The mineral phase in the solid at the end of incubation was analysed by synchrotron X-ray diffraction (SXRD). SXRD experiments were performed on beamline BL01C2 at the National Synchrotron Radiation Research Centre (NSRRC). SXRD data were collected with a double crystal monochromator radiation (λ = 0.774908 Å). A LaB_6 standard was used for calibration, and the beam size at sample was 0.9 × 0.2 mm. To

compare with the diffractograms of reference minerals, the SXRD patterns were converted to conventional Cu Kα wavelength (1.540 Å) using FIT2D program.

7. **Geochemical Modelling:**
The Act2 program of the GEOCHEMIST'S WORKBENCH modelling package was used to calculate the reaction path models by using a modified version of the Lawrence Livermore National Laboratory thermodynamic database (O'Day *et al*., 2004) augmented with thermodynamic data for Sb (Filella and May, 2003), As (Helz and Tossell, 2008), W (Mohajerin *et al*., 2014) and Mo species (Liu *et al*., 2020). The activities of these metal(loid)s are set as 10 µM and 1 µM, respectively. The equilibrium constants for the reactions used in these models are listed in the Table S-3.

Results and Discussion

1. The preference of goethite as electron acceptor than S^0:

The preference for electron acceptor is determined by the free energy gain (ΔG_r) of the redox reaction (Peiffer *et al*., 2021). The ΔG_r with goethite as the electron acceptor (blue line in Fig. S-3) is higher than that with S^0 (red line in Fig. S-3), indicating that goethite is energetically favourable as the electron acceptor over S^0. According to the redox ladder concept (Peiffer *et al*., 2021), goethite would be consumed first; after goethite is depleted, MR-1 would then use S^0 as the electron acceptor. In contrast, MR-1 prefers to reduce S^0 rather than goethite under mildly alkaline conditions, consistent with our previous study (Ye *et al*., 2022).

2. Oxidation of Sb^{III}-O to Sb^{V}-O:

The linear combination fitting (LCF) results suggest that 51 ± 1 % Sb^{III}-O was oxidised to Sb^{V}-O in the abiotic control (Goe-Sb^{III}+S^0, Table S-4). The abiotic oxidation may be attributed to the electron transfer between Sb^{III}-O and goethite *via* $O_2^{\bullet-}$ and •OH radicals (Yin *et al*., 2021). By comparison, the lower amount of Sb^{V}-O in MR-1+Goe-Sb^{III}+S^0 (39 ± 2 %) suggested that MR-1 slightly inhibited the oxidation of Sb^{III}-O, which may due to the reduction of $O_2^{\bullet-}$ and •OH radicals by the excreted electrons from MR-1 (Reguera *et al*., 2005). On the other hand, a recent study suggested that the electron transfer mediates the formation of labile Fe(III), which is more reactive than Fe(III) (Sheng *et al*., 2020). We hypothesised that the labile Fe(III) may be also involved in the oxidation of adsorbed Sb^{III}-O.

3. Transformation of Fe and S species in the solid phase:

Fe K-edge XANES suggests that Fe phase remained as 100 % goethite in the abiotic control (Goe-Sb^{III}+S^0), and only 1 % goethite were transformed to mackinawite in the presence of MR-1 (Fig. S-6 and Table S-5). Previous studies indicated that aqueous Fe(II) catalyses the transformation of iron oxides to more-crystalline forms *via* the electron transfer and Fe atom exchange between adsorbed Fe(II) and structural Fe(III) (Sheng *et al*., 2020; Liu *et al*., 2021;). Since goethite, a stable crystalline Fe(III) phase, was the initial mineral in our study, the Fe(II)-induced phase transformations was not significant (Liu *et al*., 2021).Consistent with the Sb L_I- and Fe K-edge XANES analysis, S K-edge XANES also suggested the minor formation of sulfides, including Sb and Fe sulfides (3 ± 2 % Sb_2S_3 and 4 ± 1 % pyrite) in MR-1+Goe-Sb^{III}+S^0 (Figure S-6 and Table S-6).

Although previous studies suggested that the newly formed iron sulfides can re-adsorb or precipitate with Sb-O (Burton *et al*., 2020), but its amount was too low to account for the decrease of dissolved Sb in our experiment. In detail, about 4.30 ± 0.48 µmol Sb was precipitated as Sb_2S_3, and the total sulfides was about 6.8 ± 0.9 µmol (Table S-2), therefore, the amount of Fe sulfides was <0.5 µmol. Actually, the formation of Sb_2S_3 was responsible for the loss of 1.52 ± 0.62 µmol dissolved Sb.

SXRD further confirmed the negligible transformation of Fe and S species in the solid. In detail, no newly formed minerals were observed, and goethite and rhombic S_8 were the identified minerals in both Goe-Sb^{III}+S^0 and MR-1+Goe-Sb^{III}+S^0 samples at the end of incubation (Fig. 2b). The negligible transformation of Fe and S species can be attributed to the stability of goethite and rhombic S_8.

Supplementary Tables

Table S-1 The concentrations of S^0 and polysulfides in solid-phases (blue shading, μmol/kg) and water (green shading, μmol/L) from the literature. Data were selected from those with the highest concentrations.

Environments	$[S^0]$	$[S_n^{2-}]^a$	$[HS^-]$	pH	References
Sediment ecosystems	60000	12,000	800	7.0	(van Gemerden *et al*., 1989)
Paddy soil	9375	-	-	-	(Zhang *et al*., 2019)
Sediment	9300	-	1000	-	(Zopfi *et al*., 2008)
Agricultural soil	6250	-	-	-	(Fuentes-Lara *et al*., 2019)
Sediment	1500	45	4000	-	(Holmkvist *et al*., 2011)
Sediment	300	-	-	-	(Lichtschlag *et al*., 2013)
Sediment	98	27.7	273	8.0-8.3	(Kamyshny and Ferdelman, 2010)
Subtidal sediment	60	30	160	8.3	(Luther *et al*., 2001)
Estuarine sediment	11.4	55.6	5.3	7.0	(Rozan *et al*., 2000)
Sediment ecosystems	-	393,000	500	7.8-8.5	(Visscher *et al*., 1990)
Underground spring	555	330	800	7.6	(Boulegue, 1977)
Water column	140	-	760	-	(Ciglenečki *et al*., 1996)
Pore water	100	120	2500	8.0	(Lichtschlag *et al*., 2013)
Deep Water	33	-	689	5.1	(Findlay *et al*., 2014)
Aquifer	24.1	4610	1010	6.87	(Kamyshny *et al*., 2008)
Pore water	9.2	-	15.3	5.8-6.4	(Wang and Tessier, 2009)
Hot brines	5	1060	590	6.4	(Boulegue, 1978)
Lake	-	1000	~6000	-	(Bura-Nakić *et al*., 2009)
Pore waters	-	330	5460	7.2	(Boulegue *et al*., 1982)
Pore waters	-	326	3360	6.8	(Luther *et al*., 1986)

[a] Polysulfides $[S_n^{2-}]$ are formed by the reaction between sulfide and S^0.

Table S-2 The concentration and amount of Fe(II) and sulfide at the end of incubation in Goe-Sb^{III}+S^0+MR-1. The accepted electrons of goethite and S^0 were also calculated, respectively.

		Fe(II)	Sulfide
Solution	Conc. (μM)[a]	527.2 ± 26.6	2.2 ± 0.4
	Amount (μmol)[b]	105.4 ± 5.3	0.4 ± 0.1
Solid	Conc. (μmol/g)[c]	2.7 ± 0.5	26.6 ± 3.4
	Amount (μmol)[d]	0.7 ± 0.1	6.8 ± 0.9
Total	Amount (μmol)[e]	106.1 ± 5.3	7.2 ± 0.8
Accepted electrons (μmol)[f]		106.1±5.3	14.4 ± 1.6

[a] Data from Figure 1 (at 192 h);
[b] Amount (μmol) = Conc. × volume (0.2 L);
[c] Data detected according to "Fe, S and Sb Speciation Analysis" in the Methods section;
[d] Amount (μmol) = Conc. × mass (0.255 g),
mass = initial mass (0.2 g goethite + 0.064 g S^0) − dissolution of goethite (0.009 g);
[e] Total amount (μmol) = amount in solution + amount in solid;
[f] Accepted electrons (μmol) = total amount (μmol) × 1 for Fe(II), and × 2 for sulfide.

Table S-3 Equilibrium constants for the reactions used in the reaction models.

Reaction	log*K*
$Sb(OH)_2^+ + H_2O = Sb(OH)_3 + H^+$	−1.4900
$H_2SbSO_2^- + H_2O = Sb(OH)_3 + HS^-$	−0.8768
$Sb(OH)_4^- + H^+ = Sb(OH)_3 + H_2O$	11.9200
$H_2Sb_2S_2O_2 + 4H_2O = 2Sb(OH)_3 + 2HS^- + 2H^+$	−29.8636
$H_2Sb_2S_4 + 6H_2O = 2Sb(OH)_3 + 4HS^- + 4H^+$	−50.2872
$HSb_2S_4^- + 6H_2O = 2Sb(OH)_3 + 4HS^- + 3H^+$	−46.7872
$Sb_2S_4^{2-} + 6H_2O = 2Sb(OH)_3 + 4HS^- + 2H^+$	−35.3272
$SbS_2^- + 3H_2O = Sb(OH)_3 + 2HS^- + H^+$	−20.1136
$Sb_2O_3 + 3H_2O = 2Sb(OH)_3$	−8.9600
$Sb_4O_6 + 6H_2O = 4Sb(OH)_3$	−19.6896
Stibnite + $6H_2O = 2Sb(OH)_3 + 3HS^- + 3H^+$	−53.1100
$As(OH)_3 + H_2O = As(OH)_4^- + H^+$	−9.2327
$HAsO_3^{2-} + H_2O + H^+ = As(OH)_4^-$	11.0123
$AsS_2^- + 4H_2O = As(OH)_4^- + HS^- + 2H^+$	−26.8053
$H_2AsS_2O^- + 3H_2O = As(OH)_4^- + 2HS^- + 2H^+$	−23.6327
$H_2AsS_3^- + 4H_2O = As(OH)_4^- + 3HS^- + 3H^+$	−36.1827
$H_2AsSO_2^- + 2H_2O = As(OH)_4^- + HS^- + H^+$	−12.8827
$H_3AsS_2O + 3H_2O = As(OH)_4^- + 2HS^- + 3H^+$	−27.3327
$H_3AsS_3 + 4H_2O = As(OH)_4^- + 3HS^- + 4H^+$	−39.8827
$H_3AsSO_2 + 2H_2O = As(OH)_4^- + HS^- + 2H^+$	−16.5827
$HAsS_2 + 4H_2O = As(OH)_4^- + 2HS^- + 3H^+$	−30.5068
$HAsS_2O^{2-} + 3H_2O = As(OH)_4^- + 2HS^- + H^+$	−15.0327
$HAsS_3^{2-} + 4H_2O = As(OH)_4^- + 3HS^- + 2H^+$	−27.5827
$HAsSO_2^{2-} + 2H_2O = As(OH)_4^- + HS^-$	1.2173
Arsenolite + $5H_2O = 2As(OH)_4^- + 2H^+$	−19.8859

Table S-3 continued

Reaction	log*K*
$Claudetite + 5H_2O = 2As(OH)_4^- + 2H^+$	−20.0163
$Orpiment + 8H_2O = 2As(OH)_4^- + 3HS^- + 5H^+$	−64.7654
$H_2Mo_6O_{21}^{4-} + 3H_2O = 6MoO_4^{2-} + 8H^+$	−51.1700
$H_3Mo_8O_{28}^{5-} + 4H_2O = 8MoO_4^{2-} + 11H^+$	−69.7400
$HMo_7O_{24}^{5-} + 4H_2O = 7MoO_4^{2-} + 9H^+$	−58.5800
$HMoO_4^- = MoO_4^{2-} + H^+$	−4.2400
$Mo_7O_{24}^{6-} + 4H_2O = 7MoO_4^{2-} + 8H^+$	−52.8600
$Mo_8O_{26}^{4-} + 6H_2O = 8MoO_4^{2-} + 12H^+$	−74.3800
$MoO_3(H_2O)_3 = MoO_4^{2-} + HS^- + 2H^+$	−8.2400
$MoSO_3^{2-} + H_2O = MoO_4^{2-} + HS^- + H^+$	−12.1317
$MoS_2O_2^{2-} + 2H_2O = MoO_4^{2-} + 2HS^- + 2H^+$	−23.8734
$MoS_3O^{2-} + 3H_2O = MoO_4^{2-} + 3HS^- + 3H^+$	−35.8151
$MoS_4^{2-} + 4H_2O = MoO_4^{2-} + 4HS^- + 4H^+$	−47.6368
$H_2MoO_4 = MoO_4^{2-} + 2H^+$	−12.8765
$MoO_3 + H_2O = MoO_4^{2-} + 2H^+$	−8.0000
$H_2W_{12}O_{42}^{10-} + 6H_2O = 12WO_4^{2-} + 14H^+$	−111.5000
$H_2W_6O_{22}^{6-} + 2H_2O = 6WO_4^{2-} + 6H^+$	−48.4000
$HW_7O_{24}^{5-} + 4H_2O = 7WO_4^{2-} + 9H^+$	−71.2400
$HWO_4^- = WO_4^{2-} + H^+$	−3.6200
$W_7O_{24}^{6-} + 4H_2O = 7WO_4^{2-} + 8H^+$	−65.1900
$WO_3(H_2O)_3 = WO_4^{2-} + 2H^+$	−8.7000
$H_2WO_4 = WO_4^{2-} + 2H^+$	−5.8000
$WO_3S^{2-} + H_2O = WO_4^{2-} + HS^- + H^+$	−10.0217
$WO_2S_2^{2-} + 2H_2O = WO_4^{2-} + 2HS^- + 2H^+$	−20.1834
$WOS_3^{2-} + 3H_2O = WO_4^{2-} + 3HS^- + 3H^+$	−29.8851
$WS_4^{2-} + 4H_2O = WO_4^{2-} + 4HS^- + 4H^+$	−39.1868
$H_2WO_4 = WO_4^{2-} + 2H^+$	−15.4000
$Pb(HS)_2 = Pb^{2+} + 2HS^-$	−15.2700
$Pb(HS)_3^- = Pb^{2+} + 3HS^-$	−16.5700
$Pb(OH)_2 + 2H^+ = Pb^{2+} + 2H_2O$	17.0940
$Pb(OH)_3^- + 3H^+ = Pb^{2+} + 3H_2O$	28.0910
$Pb_2(OH)^{3+} + H^+ = 2Pb^{2+} + H_2O$	6.3970
$Pb_3(OH)_4^{2+} + 4H^+ = 3Pb^{2+} + 4H_2O$	23.8880
$Pb_4(OH)_4^{4+} + 4H^+ = 4Pb^{2+} + 4H_2O$	20.8880
$Pb(OH)^+ + H^+ = Pb^{2+} + H_2O$	7.5970
$Galena + H^+ = Pb^{2+} + HS^-$	−14.9200
$Litharge + 2H^+ = Pb^{2+} + H_2O$	12.6900
$Massicot + 2H^+ = Pb^{2+} + H_2O$	12.8900
$Pb(OH)_2 + 2H^+ = Pb^{2+} + 2H_2O$	8.1500
$Pb_2O(OH)_2 + 4H^+ = 2Pb^{2+} + 3H_2O$	26.1900
$Hg(HS)_2 + 2H_2O = Hg(OH)_2 + 2HS^- + 2H^+$	−44.5800
$Hg^{2+} + 2H_2O = Hg(OH)_2 + 2H^+$	−6.1640

Table S-3 continued

Reaction	log*K*
$Hg_2(OH)^{3+} + 3H_2O = 2Hg(OH)_2 + 3H^+$	−9.0310
$Hg_3(OH)_3^{3+} + 3H_2O = 3Hg(OH)_2 + 3H^+$	−12.1010
$HHgS_2^- + 2H_2O = Hg(OH)_2 + 2\,HS^- + H^+$	−38.0900
$HgOH^+ + H_2O = Hg(OH)_2 + H^+$	−2.7670
$HgS_2^{2-} + 2H_2O = Hg(OH)_2 + 2HS^-$	−29.3800
Cinnabar + $2H_2O = Hg(OH)_2 + HS^- + H^+$	−45.2800
Metacinnabar + $2H_2O = Hg(OH)_2 + HS^- + H^+$	−44.8800
Montroydite + $H_2O = Hg(OH)_2$	−3.6100
$Zn(OH)_2 + 2H^+ = Zn^{2+} + 2H_2O$	16.8940
$Zn(OH)_3^- + 3H^+ = Zn^{2+} + 3H_2O$	28.3910
$Zn(OH)_4^- + 4H^+ = Zn^{2+} + 4H_2O$	41.1880
$Zn_2(OH)^{3+} + H^+ = 2Zn^{2+} + H_2O$	8.9970
$Zn_2S_3^{2-} + 3H^+ = 2Zn^{2+} + 3HS^-$	−0.3500
$Zn_4S_6^{4-} + 6H^+ = 4Zn^{2+} + 6HS^-$	−1.9300
$ZnOH^+ + H^+ = Zn^{2+} + H_2O$	8.9970
Spharelite + $H^+ = Zn^{2+} + HS^-$	−10.8200
Wurtzite + $H^+ = Zn^{2+} + HS^-$	−8.6200
Zincite + $2H^+ = Zn^{2+} + H_2O$	11.2300
$Cd(HS)_2 = Cd^{2+} + 2HS^-$	−15.3100
$Cd(HS)_3^- = Cd^{2+} + 3HS^-$	−17.1100
$Cd(HS)_4^{2-} = Cd^{2+} + 4HS^-$	−19.3100
$Cd(OH)_2 + 2H^+ = Cd^{2+} + 2H_2O$	20.2940
$Cd(OH)_3^- + 3H^+ = Cd^{2+} + 3H_2O$	33.3000
$Cd(OH)_4^{2-} + 4H^+ = Cd^{2+} + 4H_2O$	47.2880
$Cd_2(OH)^{3+} + H^+ = 2Cd^{2+} + H_2O$	9.3970
$CdHS^+ = Cd^{2+} + HS^-$	−8.0100
$CdOH^+ + H^+ = Cd^{2+} + H_2O$	10.0970
$Cd(OH)_2 + 2H^+ = Cd^{2+} + 2H_2O$	13.6440
Greenockite + $H^+ = Cd^{2+} + HS^-$	−14.0200

Table S-4 Linear combination fitting results of Sb XANES normalised first derivative spectra.

	Goe-Sb^{III}+S^0	**MR-1+Goe-Sb^{III}+S^0**
Sb^{III}-O	44 (2)	25 (3)
Sb^{V}-O	51 (1)	39 (2)
Sb_2S_3	5 (2)	36 (4)
R-factor	0.1588	0.2675
Chi-square	0.2780	0.7965
Reduced chi-square	0.0015	0.0042

Table S-5 Linear combination fitting results of Fe XANES normalised first derivative spectra.

	Goe-Sb^{III}+S^0	**MR-1+Goe-Sb^{III}+S^0**
Goethite	100 (0)	99 (0)
Mackinawite	0 (0)	1 (1)
Pyrite	0 (0)	0 (1)
R-factor	0.0009	0.0010
Chi-square	0.0007	0.0008
Reduced chi-square	0.0001	0.0001

Table S-6 Linear combination fitting results of sulfur XANES normalised first derivative spectra.

	Goe-Sb^{III}+S^0	**MR-1+Goe-Sb^{III}+S^0**
S^0	98 (0)	87 (1)
Cysteine	2 (0)	6 (0)
Sb_2S_3	0 (0)	3 (2)
Pyrite	0 (0)	4 (1)
R-factor	0.0037	0.0034
Chi-square	0.0118	0.0110
Reduced chi-square	0.0001	0.0001

Table S-7 Sulfide and Fe(II) concentrations (μM) in mildly acidic environments.

Environment	pH	Dissolved Sulfide	Dissolved Fe(II)	Site	References
Paddy soil	7.0	<3	286	Sacramento Valley, USA	(Tanji *et al*., 2003)
	6.2	4	31	Wanshan, China	(Rothenberg and Feng, 2012)
	6.5	200	-	Guangxi, China	(Wang *et al*., 2019)
	6.5	2	1700	Huanning, China	(G. Wang *et al*., 2020)
	6.4	3.0	300	Veronica, Italy	(J.J. Wang *et al*., 2020)
	6.4	0.3	900	Langosco, Italy	(J.J. Wang *et al*., 2020)
	6.5	1.2	1500	Cascina Oschiena, Italy	(J.J. Wang *et al*., 2020)
	6.6	1.2	100	Rovasenda, Italy	(J.J. Wang *et al*., 2020)
	6.8	0.3	700	Vedeau, France	(J.J. Wang *et al*., 2020)
Wetland	6.8	<20	-	Sepetiba Bay, Brazil	(Lacerda *et al*., 1993)
	6.5	37.5	-	Madisonville, USA	(Baldwin and Mendelssohn, 1998)
	6.8	209	-	Madisonville, USA	(Baldwin and Mendelssohn, 1998)
	6.6	<10	50	Michigan, USA	(Koretsky *et al*., 2006)
	6.5	150	< 10	Michigan, USA	(Koretsky *et al*., 2007)
	6.5	25	30	Michigan, USA	(Koretsky *et al*., 2007)
	6.5	10	100	Michigan, USA	(Koretsky *et al*., 2007)
	6.5	<5	50	Michigan, USA	(Koretsky *et al*., 2007)
	6.0	<2	40,000	North-eastern Australia	(Burton *et al*., 2011)
	6.4	25	-	Weeks Bay, USA	(Lee *et al*., 2019)
	6.58	<1	230	Min River Estuary, China	(Luo *et al*., 2019)
	6.4	0.8	-	Lake Angessjon, Sweden	(Skyllberg *et al*., 2021)
	6.6	2.6	86.5	New York, USA	(Simkin *et al*., 2021)
	6.6	13.3	17.7	New York, USA	(Simkin *et al*., 2021)
Groundwater	5.9	0.3	6.25	Titas district, Bangladesh	(Planer-Friedrich *et al*., 2018)
	6.5	0.3	7.7	Titas district, Bangladesh	(Planer-Friedrich *et al*., 2018)
	6.5	0.3	6.6	Titas district, Bangladesh	(Planer-Friedrich *et al*., 2018)
	6.8	0.6	36.6	Titas district, Bangladesh	(Planer-Friedrich *et al*., 2018)
	6.3	0.3	957	Titas district, Bangladesh	(Planer-Friedrich *et al*., 2018)
	6.4	0.3	1589	Titas district, Bangladesh	(Planer-Friedrich *et al*., 2018)
	6.4	-	960	Titas district, Bangladesh	(Planer-Friedrich *et al*., 2018)
	6.3	0.3	754	Titas district, Bangladesh	(Planer-Friedrich *et al*., 2018)
	6.3	0.6	848	Titas district, Bangladesh	(Planer-Friedrich *et al*., 2018)
	6.4	-	625	Titas district, Bangladesh	(Planer-Friedrich *et al*., 2018)
	6.2	-	1107	Titas district, Bangladesh	(Planer-Friedrich *et al*., 2018)
	6.2	-	1911	Titas district, Bangladesh	(Planer-Friedrich *et al*., 2018)
	6.3	0.9	991	Titas district, Bangladesh	(Planer-Friedrich *et al*., 2018)
	6.2	0.3	1500	Titas district, Bangladesh	(Planer-Friedrich *et al*., 2018)
	6.3	-	1036	Titas district, Bangladesh	(Planer-Friedrich *et al*., 2018)
	6.3	0.6	839	Titas district, Bangladesh	(Planer-Friedrich *et al*., 2018)

Table S-7 continued

Environment	pH	Dissolved Sulfide	Dissolved Fe(II)	Site	References
Groundwater	6.3	-	2196	Titas district, Bangladesh	(Planer-Friedrich *et al*., 2018)
	6.3	0.9	2143	Titas district, Bangladesh	(Planer-Friedrich *et al*., 2018)
	6.5	0.6	2804	Titas district, Bangladesh	(Planer-Friedrich *et al*., 2018)
	6.5	-	25	Titas district, Bangladesh	(Planer-Friedrich *et al*., 2018)
	6.4	-	147	Titas district, Bangladesh	(Planer-Friedrich *et al*., 2018)
	6.6	0.3	187.5	Titas district, Bangladesh	(Planer-Friedrich *et al*., 2018)
	6.5	0.3	295	Titas district, Bangladesh	(Planer-Friedrich *et al*., 2018)
	6.5	0.9	317	Titas district, Bangladesh	(Planer-Friedrich *et al*., 2018)
	6.5	1.3	295	Titas district, Bangladesh	(Planer-Friedrich *et al*., 2018)
	6.5	0.3	333	Titas district, Bangladesh	(Planer-Friedrich *et al*., 2018)
	6.5	0.1	440	Titas district, Bangladesh	(Planer-Friedrich *et al*., 2018)
Lake/River	>6.5	0.17	120	Lake Matano, Sulawesi	(Crowe *et al*., 2008)
	6.8	260	-	New York, USA	(Oduro *et al*., 2013)
	6.7	1060	-	New York, USA	(Oduro *et al*., 2013)
	6.4	0.3	-	Kedah and Terengganu, Malaysia	(Amal *et al*., 2015)
	6.5	5	50	Quebec, Canada	(Couture *et al*., 2016)
	6.9	2	600	Quebec, Canada	(Couture *et al*., 2016)
	6.5	2.8	27	Becker, USA	(Pollman *et al*., 2017)
	6.3	3.3	305	St. Louis, USA	(Pollman *et al*., 2017)
	6.4	80	<0.2	Freeborn, USA	(Pollman *et al*., 2017)
	6.5	14	0.55	Itasca, USA	(Pollman *et al*., 2017)

Supplementary Figures

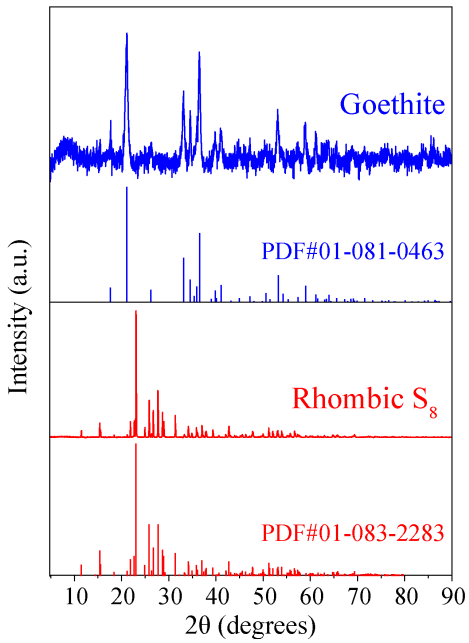

Figure S-1 X-ray powder diffraction pattern recorded from goethite and rhombic S_8 used in this study.

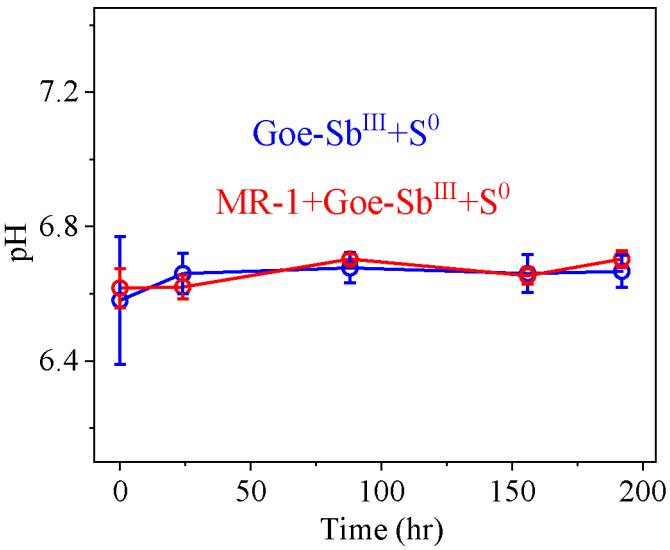

Figure S-2 Change in pH values as a function of incubation time in Goe-Sb^{III}+S^0 (blue) and Goe-Sb^{III}+S^0+MR-1 (red).

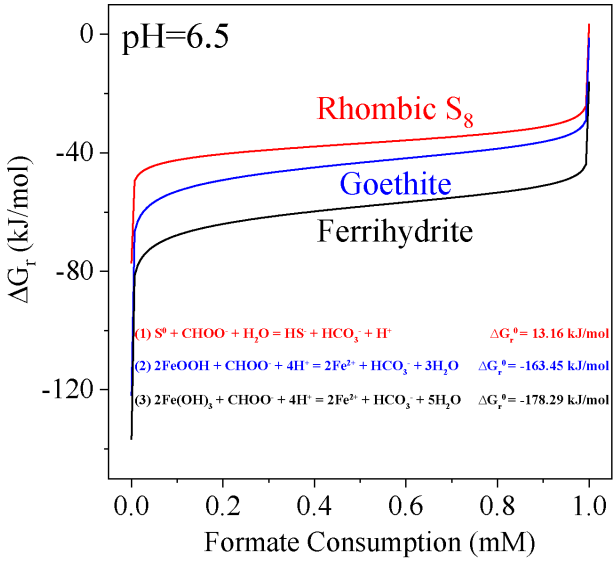

Figure S-3 Free energy change with the consumption of formate when rhombic S_8 (red), goethite (blue) and ferrihydrite (black) as the electron acceptor, respectively. The insert shows the standard Gibbs free energies change (ΔG_r^0) of the redox reactions. The initial formate concentration was set as 1 mM and pH was set as 6.5. Thermodynamic data used for calculation are from a previous study (Haynes, 2015).

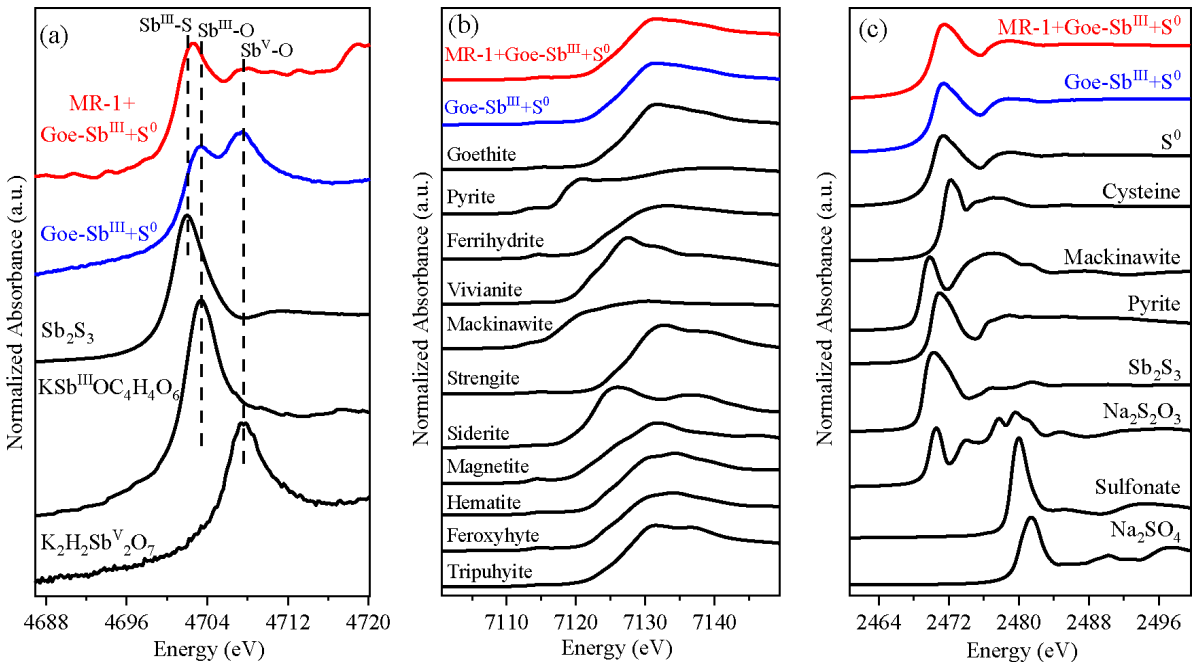

Figure S-4 Normalised **(a)** Sb L_I-, **(b)** Fe and **(c)** S K-edge XANES for samples at the end of incubation. Spectra for standard references are also shown for comparison.

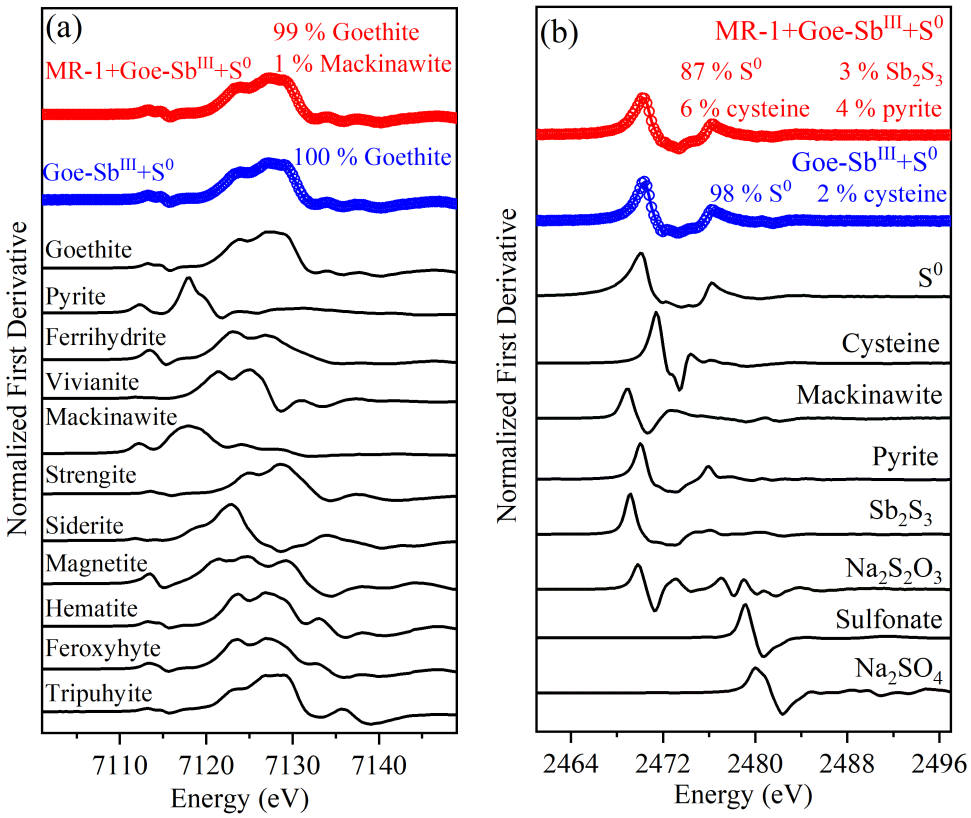

Figure S-5 Observed (circles) and linear combination fitting (lines) for the first derivative of normalised **(a)** Fe and **(b)** S K-edge XANES for samples at the end of incubation. Spectra for standard references are also shown for comparison. The results of linear combination fitting analysis are shown in Tables S-5 and S-6.

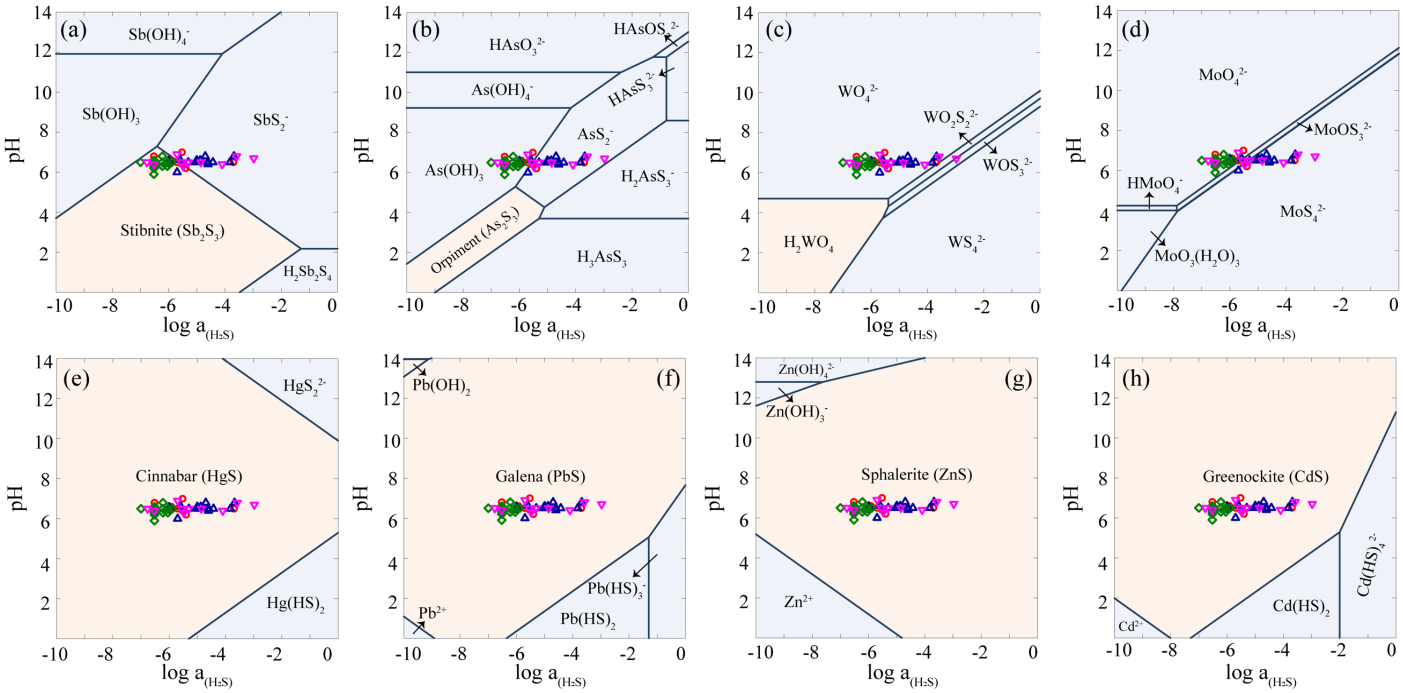

Figure S-6 Species of **(a)** Sb, **(b)** As, **(c)** W, **(d)** Mo, **(e)** Hg, **(f)** Pb, **(g)** Zn and **(h)** Cd in the reaction with different log activity (H_2S) and pH values in the presence of goethite at 25 °C. The activities of these metal(loid)s were set as 1 μM. The red, blue, green and magenta symbols represent the sulfide concentrations in mildly acidic paddy, wetland, groundwater and lake/river systems, respectively. The data are from references in Table S-7.

Supplementary Information References

Amal, M.N.A., Saad, M.Z., Zahrah, A.S., Zulkafli, A.R. (2015) Water quality influences the presence of *Streptococcus agalactiae* in cage cultured red hybrid tilapia, *Oreochromis niloticus* × *Oreochromis mossambicus*. *Aquaculture Research* 46, 313–323. https://doi.org/10.1111/are.12180

Baldwin, A.H., Mendelssohn, I.A. (1998) Effects of salinity and water level on coastal marshes: an experimental test of disturbance as a catalyst for vegetation change. *Aquatic Botany* 61, 255–268. https://doi.org/10.1016/S0304-3770(98)00073-4

Boulegue, J. (1977) Equilibria in a sulfide rich water from Enghien-les-Bains, France. *Geochimica et Cosmochimica Acta* 41, 1751–1758. https://doi.org/10.1016/0016-7037(77)90207-1

Boulegue, J. (1978) Metastable sulfur species and trace-metals (Mn, Fe, Cu, Zn, Cd, Pb) in hot brines from French Dogger. *American Journal of Science* 278, 1394–1411. https://doi.org/10.2475/ajs.278.10.1394

Boulegue, J., Lord, C.J., Church, T.M. (1982) Sulfur speciation and associated trace metals (Fe, Cu) in the pore waters of Great Marsh, Delaware. *Geochimica et Cosmochimica Acta* 46, 453–464. https://doi.org/10.1016/0016-7037(82)90236-8

Bura-Nakić, E., Helz, G.R., Ciglenečki, I., Ćosović, B. (2009) Reduced sulfur species in a stratified seawater lake (Rogoznica Lake, Croatia); seasonal variations and argument for organic carriers of reactive sulfur. *Geochimica et Cosmochimica Acta* 73, 3738–3751. https://doi.org/10.1016/j.gca.2009.03.037

Burton, E.D., Bush, R.T., Johnston, S.G., Sullivan, L.A., Keene, A.F. (2011) Sulfur biogeochemical cycling and novel Fe-S mineralization pathways in a tidally re-flooded wetland. *Geochimica et Cosmochimica Acta* 75, 3434–3451. https://doi.org/10.1016/j.gca.2011.03.020

Burton, E.D., Hockmann, K., Karimian, N. (2020) Antimony sorption to goethite: Effects of Fe(II)-catalyzed recrystallization. *ACS Earth and Space Chemistry* 4, 476–487. https://doi.org/10.1021/acsearthspacechem.0c00013

Ciglenečki, I., Kodba, Z., Ćosović, B. (1996) Sulfur species in Rogoznica Lake. *Marine Chemistry* 53, 101–110. https://doi.org/10.1016/0304-4203(96)00016-3

Clesceri, L.S., Greenberg, A.E., Eaton, A.D. (Eds.). (1998) *Standard Methods for the Examination of Water and Wastewater*. 20th Edition, American Public Health Association, American Water Works Association and Water Environment Federation, Washington, D.C.

Couture, R.-M., Fischer, R., Van Cappellen, P., Gobeil, C. (2016) Non-steady state diagenesis of organic and inorganic sulfur in lake sediments. *Geochimica et Cosmochimica Acta* 194, 15–33. https://doi.org/10.1016/j.gca.2016.08.029

Crowe, S.A., Jones, C., Katsev, S., Magen, C., O'Neill, A.H., Sturm, A., Canfield, D.E., Haffner, G.D., Mucci, A., Sundby, B., Fowle, D.A. (2008) Photoferrotrophs thrive in an Archean Ocean analogue. *Proceedings of the National Academy of Sciences* 105, 15938–15943. https://doi.org/10.1073/pnas.0805313105

Filella, M., May, P.M. (2003) Computer simulation of the low-molecular-weight inorganic species distribution of antimony(III) and antimony(V) in natural waters. *Geochimica et Cosmochimica Acta* 67, 4013–4031. https://doi.org/10.1016/S0016-7037(03)00095-4

Findlay, A.J., Gartman, A., MacDonald, D.J., Hanson, T.E., Shaw, T.J., Luther, G.W., III (2014) Distribution and size fractionation of elemental sulfur in aqueous environments: The Chesapeake Bay and Mid-Atlantic Ridge. *Geochimica et Cosmochimica Acta* 142, 334–348. https://doi.org/10.1016/j.gca.2014.07.032

Fuentes-Lara, L.O., Medrano-Macias, J., Perez-Labrada, F., Rivas-Martinez, E.N., Garcia-Enciso, E.L., Gonzalez-Morales, S., Juarez-Maldonado, A., Rincon-Sanchez, F., Benavides-Mendoza, A. (2019) From elemental sulfur to hydrogen sulfide in agricultural soils and plants. *Molecules* 24, 17. https://doi.org/10.3390/molecules24122282

Haynes, W.M. (2015) *CRC Handbook of Chemistry and Physics*. 96th Edition, CRC Press/Taylor & Francis, Boca Raton.

Helz, G.R., Tossell, J.A. (2008) Thermodynamic model for arsenic speciation in sulfidic waters: A novel use of *ab initio* computations. *Geochimica et Cosmochimica Acta* 72, 4457–4468. https://doi.org/10.1016/j.gca.2008.06.018

Holmkvist, L., Kamyshny, A., Vogt, C., Vamvakopoulos, K., Ferdelman, T.G., Jørgensen, B.B. (2011) Sulfate reduction below the sulfate–methane transition in Black Sea sediments. *Deep Sea Research Part I: Oceanographic Research Papers* 58, 493–504. https://doi.org/10.1016/j.dsr.2011.02.009

Kamyshny, A., Jr., Ferdelman, T.G. (2010) Dynamics of zero-valent sulfur species including polysulfides at seep sites on intertidal sand flats (Wadden Sea, North Sea). *Marine Chemistry* 121, 17–26. https://doi.org/10.1016/j.marchem.2010.03.001

Kamyshny, A., Jr., Zilberbrand, M., Ekeltchik, I., Voitsekovski, T., Gun, J., Lev, O. (2008) Speciation of polysulfides and zerovalent sulfur in sulfide-rich water wells in southern and central Israel. *Aquatic Geochemistry* 14, 171–192. https://doi.org/10.1007/s10498-008-9031-6

Koretsky, C.M., Haas, J.R., Ndenga, N.T., Miller, D. (2006) Seasonal variations in vertical redox stratification and potential influence on trace metal speciation in minerotrophic peat sediments. *Water, Air, and Soil Pollution* 173, 373–403. https://doi.org/10.1007/s11270-006-9089-y

Koretsky, C.M., Haveman, M., Beuving, L., Cuellar, A., Shattuck, T., Wagner, M. (2007) Spatial variation of redox and trace metal geochemistry in a minerotrophic fen. *Biogeochemistry* 86, 33–62. https://doi.org/10.1007/s10533-007-9143-x

Lacerda, L.D., Carvalho, C.E.V., Tanizaki, K.F., Ovalle, A.R.C., Rezende, C.E. (1993) The biogeochemistry and trace-metals distribution of mangrove rhizospheres. *Biotropica* 25, 252–257. https://doi.org/10.2307/2388783

Lee, P.O., Shoemaker, C., Olson, J.B. (2019) Wetland soil properties and resident bacterial communities are influenced by changes in elevation. *Wetlands* 39, 99–112. https://doi.org/10.1007/s13157-018-1077-7

Lichtschlag, A., Kamyshny, A., Ferdelman, T.G., deBeer, D. (2013) Intermediate sulfur oxidation state compounds in the euxinic surface sediments of the Dvurechenskii mud volcano (Black Sea). *Geochimica et Cosmochimica Acta* 105, 130–145. https://doi.org/10.1016/j.gca.2012.11.025

Liu, C.S., Massey, M.S., Latta, D.E., Xia, Y.F., Li, F.B., Gao, T., Hua, J. (2021) Fe(II)-induced transformation of iron minerals in soil ferromanganese nodules. *Chemical Geology* 559, 119901. https://doi.org/10.1016/j.chemgeo.2020.119901

Liu, W., Etschmann, B., Mei, Y., Guan, Q., Testemale, D., Brugger, J. (2020) The role of sulfur in molybdenum transport in hydrothermal fluids: Insight from *in situ* synchrotron XAS experiments and molecular dynamics simulations. *Geochimica et Cosmochimica Acta* 290, 162–179. https://doi.org/10.1016/j.gca.2020.08.003

Luo, M., Zhu, W., Huang, J., Liu, Y., Duan, X., Wu, J., Tong, C. (2019) Anaerobic organic carbon mineralization in tidal wetlands along a low-level salinity gradient of a subtropical estuary: Rates, pathways, and controls. *Geoderma* 337, 1245–1257. https://doi.org/10.1016/j.geoderma.2018.07.030

Luther, G.W., Church, T.M., Scudlark, J.R., Cosman, M. (1986) Inorganic and organic sulfur cycling in salt-marsh pore waters. *Science* 232, 746–749. https://doi.org/10.1126/science.232.4751.746

Luther, G.W., Glazer, B.T., Hohmann, L., Popp, J.I., Taillefert, M., Rozan, T.F., Brendel, P.J., Theberge, S.M., Nuzzio, D.B. (2001) Sulfur speciation monitored *in situ* with solid state gold amalgam voltammetric microelectrodes: polysulfides as a special case in sediments, microbial mats and hydrothermal vent waters. *Journal of Environmental Monitoring* 3, 61–66. https://doi.org/10.1039/b006499h

Mohajerin, T.J., Helz, G.R., White, C.D., Johannesson, K.H. (2014) Tungsten speciation in sulfidic waters: Determination of thiotungstate formation constants and modeling their distribution in natural waters. *Geochimica et Cosmochimica Acta* 144, 157–172. https://doi.org/10.1016/j.gca.2014.08.037

O'Day, P.A., Vlassopoulos, D., Root, R., Rivera, N. (2004) The influence of sulfur and iron on dissolved arsenic concentrations in the shallow subsurface under changing redox conditions. *Proceedings of the National Academy of Sciences* 101, 13703–13708. https://doi.org/10.1073/pnas.0402775101

Oduro, H., Kamyshny, A., Jr., Zerkle, A.L., Li, Y., Farquhar, J. (2013) Quadruple sulfur isotope constraints on the origin and cycling of volatile organic sulfur compounds in a stratified sulfidic lake. *Geochimica et Cosmochimica Acta* 120, 251–262. https://doi.org/10.1016/j.gca.2013.06.039

Peiffer, S., Kappler, A., Haderlein, S.B., Schmidt, C., Byrne, J.M., Kleindienst, S., Vogt, C., Richnow, H.H., Obst, M., Angenent, L.T., Bryce, C., McCammon, C., Planer-Friedrich, B. (2021) A biogeochemical–hydrological framework for the role of redox-active compounds in aquatic systems. *Nature Geoscience* 14, 264–272. https://doi.org/10.1038/s41561-021-00742-z

Planer-Friedrich, B., Schaller, J., Wismeth, F., Mehlhorn, J., Hug, S.J. (2018) Monothioarsenate occurrence in Bangladesh groundwater and its removal by ferrous and zero-valent iron technologies. *Environmental Science & Technology* 52, 5931–5939. https://doi.org/10.1021/acs.est.8b00948

Pollman, C.D., Swain, E.B., Bael, D., Myrbo, A., Monson, P., Shore, M.D. (2017) The evolution of sulfide in shallow aquatic ecosystem sediments: An analysis of the roles of sulfate, organic carbon, and iron and feedback constraints using

structural equation modeling. *Journal of Geophysical Research: Biogeosciences* 122, 2719–2735. https://doi.org/10.1002/2017JG003785

Reguera, G., McCarthy, K.D., Mehta, T., Nicoll, J.S., Tuominen, M.T., Lovley, D.R. (2005) Extracellular electron transfer via microbial nanowires. *Nature* 435, 1098–1101. https://doi.org/10.1038/nature03661

Rothenberg, S.E., Feng, X. (2012) Mercury cycling in a flooded rice paddy. *Journal of Geophysical Research: Biogeosciences* 117, G03003. https://doi.org/10.1029/2011JG001800

Rozan, T.F., Theberge, S.M., Luther, G. (2000) Quantifying elemental sulfur (S^0), bisulfide (HS^-) and polysulfides (S_x^{2-}) using a voltammetric method. *Analytica Chimica Acta* 415, 175–184. https://doi.org/10.1016/S0003-2670(00)00844-8

Sheng, A., Liu, J., Li, X., Qafoku, O., Collins, R.N., Jones, A.M., Pearce, C.I., Wang, C., Ni, J., Lu, A., Rosso, K.M. (2020) Labile Fe(III) from sorbed Fe(II) oxidation is the key intermediate in Fe(II)-catalyzed ferrihydrite transformation. *Geochimica et Cosmochimica Acta* 272, 105–120. https://doi.org/10.1016/j.gca.2019.12.028

Simkin, S.M., Bedford, B.L., Weathers, K.C. (2021) Regional wetland plant responses to sulfur and other porewater chemistry in calcareous rich fens. *Wetlands* 41, 42. https://doi.org/10.1007/s13157-021-01438-1

Skyllberg, U., Persson, A., Tjerngren, I., Kronberg, R.-M., Drott, A., Meili, M., Bjorn, E. (2021) Chemical speciation of mercury, sulfur and iron in a dystrophic boreal lake sediment, as controlled by the formation of mackinawite and framboidal pyrite. *Geochimica et Cosmochimica Acta* 294, 106–125. https://doi.org/10.1016/j.gca.2020.11.022

Tanji, K.K., Gao, S., Scardaci, S.C., Chow, A.T. (2003) Characterizing redox status of paddy soils with incorporated rice straw. *Geoderma* 114, 333–353. https://doi.org/10.1016/S0016-7061(03)00048-X

van Gemerden, H., Tughan, C.S., de Wit, R., Herbert, R.A. (1989) Laminated microbial ecosystems on sheltered beaches in Scapa Flow, Orkney Islands. *FEMS Microbiology Ecology* 5, 87–102. https://doi.org/10.1111/j.1574-6968.1989.tb03661.x

Visscher, P.T., Nijburg, J.W., van Gemerden, H. (1990) Polysulfide utilization by *Thiocapsa-roseopersicina*. *Archives of Microbiology* 155, 75–81. https://doi.org/10.1007/BF00291278

Wang, F., Tessier, A. (2009) Zero-valent sulfur and metal speciation in sediment porewaters of freshwater lakes. *Environmental Science & Technology* 43, 7252–7257. https://doi.org/10.1021/es8034973

Wang, G., Hu, Z., Li, S., Wang, Y., Sun, X., Zhang, X., Li, M. (2020) Sulfur controlled cadmium dissolution in pore water of cadmium-contaminated soil as affected by DOC under waterlogging. *Chemosphere* 240, 124846. https://doi.org/10.1016/j.chemosphere.2019.124846

Wang, J., Wang, P.-M., Gu, Y., Kopittke, P.M., Zhao, F.-J., Wang, P. (2019) Iron-manganese (oxyhydro)oxides, rather than oxidation of sulfides, determine mobilization of Cd during soil drainage in paddy soil systems. *Environmental Science & Technology* 53, 2500–2508. https://doi.org/10.1021/acs.est.8b06863

Wang, J.J., Kerl, C.F., Hu, P.J., Martin, M., Mu, T.T., Bruggenwirth, L., Wu, G.M., Said-Pullicino, D., Romani, M., Wu, L.H., Planer-Friedrich, B. (2020) Thiolated arsenic species observed in rice paddy pore waters. *Nature Geoscience* 13, 282–287. https://doi.org/10.1038/s41561-020-0533-1

Ye, L., Chen, H., Jing, C. (2019) Sulfate-reducing bacteria mobilize adsorbed antimonate by thioantimonate formation. *Environmental Science & Technology Letters* 6, 418–422. https://doi.org/10.1021/acs.estlett.9b00353

Ye, L., Meng, X., Jing, C. (2020) Influence of sulfur on the mobility of arsenic and antimony during oxic-anoxic cycles: Differences and competition. *Geochimica et Cosmochimica Acta* 288, 51–67. https://doi.org/10.1016/j.gca.2020.08.007

Yin, X.L., Zhang, G.Q., Su, R., Zeng, X.F., Yan, Z.L., Zhang, D.N., Ma, X., Lei, L., Lin, J.R., Wang, S.F., Jia, Y.F. (2021) Oxidation and incorporation of adsorbed antimonite during iron (II)-catalyzed recrystallization of ferrihydrite. *Science of The Total Environment* 778, 146424. https://doi.org/10.1016/j.scitotenv.2021.146424

Zerkle, A.L., Kamyshny, A., Jr., Kump, L.R., Farquhar, J., Oduro, H., Arthur, M.A. (2010) Sulfur cycling in a stratified euxinic lake with moderately high sulfate: Constraints from quadruple S isotopes. *Geochimica et Cosmochimica Acta* 74, 4953–4970. https://doi.org/10.1016/j.gca.2010.06.015

Zhang, D., Du, G., Chen, D., Shi, G., Rao, W., Li, X., Jiang, Y., Liu, S., Wang, D. (2019) Effect of elemental sulfur and gypsum application on the bioavailability and redistribution of cadmium during rice growth. *Science of The Total Environment* 657, 1460–1467. https://doi.org/10.1016/j.scitotenv.2018.12.057

Zopfi, J., Böttcher, M.E., Jørgensen, B.B. (2008) Biogeochemistry of sulfur and iron in *Thioploca*-colonized surface sediments in the upwelling area off central Chile. *Geochimica et Cosmochimica Acta* 72, 827–843. https://doi.org/10.1016/j.gca.2007.11.031